SPARSE SUPERPIXEL UNMIXING FOR EXPLORATORY ANALYSIS OF CRISM HYPERSPECTRAL IMAGES

D. R. Thompson, Rebecca Castaño *

Caltech Jet Propulsion Laboratory
4800 Oak Grove Dr.,
Pasadena, CA 91109

M. Gilmore, †

Wesleyan University
Wesleyan Station
Middletown, Connecticut 06459

ABSTRACT

Automated analysis of hyperspectral imagery can inform observation planning and tactical decisions during planetary exploration. Timely analysis can draft mineralogical maps to focus analysts attention on areas of interest or facilitate data mining in large hyperspectral catalogs. In this work, sparse spectral unmixing with Bayesian Positive Source Separation produces mineral abundance maps from Mars Reconnaissance Orbiter Compact Reconnaissance Imaging Spectrometer (CRISM) images. We demonstrate a novel "superpixel" segmentation strategy to enable efficient unmixing in an interactive session. Tests correlate automatic unmixing results based on redundant spectral libraries against hand-tuned indicator functions currently in use by CRISM researchers.

Index Terms— Sparse Unmixing, CRISM, Hyperspectral Images, Superpixels, Image Segmentation

1. INTRODUCTION

Planetary exploration scenarios hold special challenges for hyperspectral image analysis. With the exception of isolated landing sites there is no ground-truth compositional data from the surface. The number and character of spectral sources is unknown. A trained analyst might infer constituents through inspection, but increasing data volumes will preclude comprehensive analysis of this kind. For example, the Compact Reconnaissance Imaging Spectrometer (CRISM) aboard the Mars Reconnaissance Orbiter [1] is collecting images at unprecedented spatial and spectral resolution. It will return over a terabyte of data to Earth over its nominal mission, which is far larger than our capacity for exhaustive manual study.

Timely analysis will require techniques that automatically search an image and summarize possible constituents. With some oversimplification we can categorize current search strategies as "supervised" or "unsupervised." Supervised methods use a detection function, developed on previous data by hand or statistical techniques, to identify one or more specific target signals. For example hand-selected band ratios can reveal spectral features that are diagnostic of particular minerals [2, 3]. Other supervised detection strategies exploit classifiers such as neural networks [4] or decision trees [5]. These are suited to focused searches for specific mineral types; they may not notice unanticipated or anomalous mineralogy. The detection decision does not always generalize to new scenes and in general only detect constituents that have already been observed and for which training data is available. Alternatively, unsupervised techniques like PCA summarize the structure inherent in each new image. Purely unsupervised results are not always physically meaningful, and may ignore subtle or localized mineralogy since they aim to minimize reconstruction error over the entire image.

Here we examine a spectral unmixing approach to mineralogical search. A sparse Bayesian approach to spectral unmixing computes statistically likely combinations of constituents based on a set of possible sources with uncertain abundancess. Our approach leverages a redundant library of source spectra from laboratory experiments or previous remote observations. A "superpixel" segmentation strategy improves analysis time by orders of magnitude, permitting incorporation into an interactive user session. Preliminary tests suggest that the Bayesian spectral unmixing approach can assist analysis of CRISM data and hyperspectral imagery in general.

2. APPROACH

We use a linear mixing model where m source spectra in w wavelengths combine to yield n observations:

$$\mathbf{x}_\lambda \quad = \quad \mathbf{A}\mathbf{s}_\lambda + \mathcal{N}(0, \sigma^2) \tag{1}$$

Each wavelength λ is associated with an $n \times 1$ observation vector $\mathbf{x}_\lambda$, and an $m \times 1$ source vector $\mathbf{s}_\lambda$. Here $\mathbf{A}$ is an $n \times m$ mixing matrix whose entries describe the contribution of each source signal to the resulting observation. We assume additive zero-mean Gaussian noise of variance σ^2. More generally one can treat the entire spectrum of independent wavelengths as columns of an $m \times w$ source matrix $\mathbf{S}$ and an $n \times w$ observation matrix $\mathbf{X}$. We will index matrix entries with subscripts

* *david.r.thompson@jpl.nasa.gov, rebecca.castano@jpl.nasa.gov*
† *mgilmore@wesleyan.edu*

so that the ith observation on bandwidth λ is $\mathbf{X}_{i\lambda}$. Given source and observation matrices, the unmixing problem aims to recover the mixing matrix $\mathbf{A}$.

2.1. Sparse Bayesian Unmixing

Our geographic linear mixing model places several constraints on $\mathbf{A}$. Minerals' reflectances represent fractions of incident illumination and combine in proportion to their abundance on the imaged surface. To reflect this physical intuition, entries of A must be zero or positive. Standard non-negative unmixing strategies minimize squared reconstruction error while enforcing positivity as in Nonnegative Matrix Factorization [6]. However, in our case there is another important constraint: the source library may be highly *overcomplete*. In other words, it will certainly contain many more possible sources than actually exist in the scene. As a result we must favor *sparse* solutions where most entries of $\mathbf{A}$ are zero.

We enforce both non-negativity and sparsity using an exponential prior distribution $\mathcal{G}$ parameterized with rate hyperparameter α, on entries of the mixing matrix. From Bayes' rule:

$$p(\mathbf{A}|\mathbf{X},\alpha) \propto p(\mathbf{X}|\mathbf{A})p(\mathbf{A}|\alpha) \tag{2}$$

$$\propto \prod_{i\lambda} \mathcal{N}(\mathbf{X}_{i\lambda} - [A\mathbf{S}]_{i\lambda}, \sigma^2) \prod_{ij} \mathcal{G}(\mathbf{A}_{ij}, \alpha) \tag{3}$$

$$\propto \prod_{i\lambda} \exp\left\{\frac{-(\mathbf{X}_{i\lambda} - [A\mathbf{S}]_{i\lambda})^2}{2\sigma^2}\right\} \prod_{ij} \exp\{-\alpha\mathbf{A}_{ij}\} \tag{4}$$

We maximize this probability with an iterative gradient descent procedure similar to that described by Moussaoui *et al.* [7]. Taking $\log p(\mathbf{A}|\mathbf{x},\alpha)$ and dropping constant terms produces the objective function $\mathcal{V}(\mathbf{A})$:

$$\mathcal{V}(\mathbf{A}) \quad = \quad -\frac{1}{2\sigma^2}\sum_{i\lambda}(\mathbf{X}_{i\lambda} - [A\mathbf{S}]_{i\lambda})^2 - \sum_{ij}\alpha\mathbf{A}_{ij} \tag{5}$$

Note that this amounts to a least-squares error minimization with an L1-norm penalty term, similar to the sparsity-inducing LASSO estimator [8]. We maximize this with iterative ascent of the gradient of $\mathcal{V}(\mathbf{A})$ with respect to $\mathbf{A}$:

$$\nabla_{\mathbf{A}_{ij}}\mathcal{V}(\mathbf{A}) = [(\mathbf{X} - \mathbf{AS})\mathbf{S}^T]_{ij} - \alpha \tag{6}$$

The density of the exponential distribution is zero for negative values of $\mathbf{A}$. Our subgradient-inspired approach replaces negative gradient values with zero for entries $\mathbf{A}_{ij}$ within numerical tolerance of zero. This produces an $n \times m$ matrix $\Psi(\mathbf{A})$ representing the update direction:

$$\Psi_{ij}(\mathbf{A}) \quad = \quad \begin{cases} \nabla_{\mathbf{A}_{ij}}\mathcal{V}(\mathbf{A}) & \text{if} \mathbf{A}_{ij} \geq 0 \\ 0 & \text{otherwise} \end{cases} \tag{7}$$

The iterative update at time t follows the update direction Φ^t for the positive step size β:

$$\mathbf{A}^t = \mathbf{A}^{t-1} + \beta\Phi^t \tag{8}$$

At each step we identify the optimal step size β with a line search. Finally, we estimate the noise parameter σ from the reprojected observations as in Moussaoui *et al* [7], fitting noise and mixing parameters in turn until reaching a local optimum. This strategy generally identifies a local Maximum A Priori estimate in less than 100 iterations, permitting real-time, interactive spectral unmixing of user-selected image regions.

2.2. Image Segmentation

Segmentation provides several advantages to mineralogical search. In general we aim to draft compositional maps for large scale data mining of trends and detection of novel mineralogy. This suggests analysis of entire images containing thousands or millions of distinct spectra, but the spectral unmixing algorithm is still too slow to exhaustively unmix all pixels during an interactive session. Segmentation permits a single mean spectrum to stand in for many pixels, potentially improving run time by orders of magnitude. In addition, segmentation counters pixel-level noise that might otherwise produce false positive detections. Real (non-noise) signals generally come from objects such as outcrops that subtend several adjacent pixels in the high resolution imagery. We can exploit this fact by analyzing the mean spectra of physically-connected regions within the image.

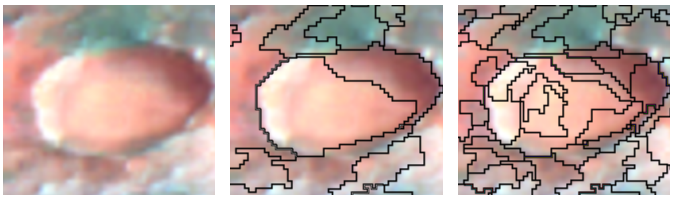

Fig. 1. Here a subwindow of observation frt0003e12 demonstrates the superpixel segmentation. Finer segmentations provide additional resolution at the cost of greater computation time and sensitivity to noise. Left: Original subimage. Center: coarse segmentation, minimum region size 100. Right: fine segmentation, minimum region size 20.

For mineralogical search important that small outlier units of surface material are given independent segments. Conversely, larger units of surface material can safely be split into multiple segments with minimal effect on performance. This leads us to intentionally oversegment the scene, a technique known in the Computer Vision community as *superpixel* segmentation. Each superpixel provides some small connected image region that is compositionally homogeneous [9]. We favor segmentations that produce 3000-5000 superpixels; unmixing them requires approximately 20 minutes to analyze a single image with a modern desktop processor.

We compute superpixels with a graph segmentation approach. We treat the grid of image pixels as an 8-connected graph of vertices and edges with a weight $d(\mathbf{X}_i, \mathbf{X}_k)$ between

neighboring pixels defined as the sum of squared differences at all wavelengths:

$$d(\mathbf{X}_i, \mathbf{X}_k) = \sum_{\lambda} (\mathbf{X}_{i\lambda} - \mathbf{X}_{k\lambda})^2 \quad (9)$$

We cluster pixels by merging them into successively larger subgraphs using the technique of Felzenszwalb *et al* [10]. The Felzenszwalb criterion merges neighboring subgraphs whenever the weight associated with their smallest connecting edge is some threshold larger than the minimum *internal* weight in either subgraph. A final postprocessing step merges regions smaller than a minimum size. Important advantages of this algorithm are efficiency and the ability to segment hyperspectral data based on a hyperspectral distance measure. Additionally it can trade speed for accuracy depending on merging thresholds and minimum region size (Figure 1). We refer the reader to [10] for details of implementation.

3. EVALUATION

A case study analyzes spectra for CRISM Infrared wavelengths from $1.0\mu m$ to $2.5\mu m$. We quantify the correlations for images FRT00003e12 and FRT00003fb9 from the Nili Fossae region (later we omit the "FRT0000" prefixes for clarity). Spectra from the first image suggest Olivine and Phyllosilicate minerals [11], while the latter also evidences a strong Olivine signature with evidence for Carbonates such as Magnesite [12]. The source matrix for image 3e12 consists of spectra drawn from the MRO/CRISM spectral library. These include 27 examples of Olivine and 59 examples of phyllosilicates such as Montmorillonite, Nontronite, Saponite, Kaolinite, and Illite. We also augment image 3fb9's library with examples of Magnesite and Hydromagnesite. This diversity helps to account for variation within mineral species. We $L1$-normalize all source spectra during unmixing so that a common hyperparameter α affects all sources equally. Finally, we append 10 featureless line spectra to the library to compensate for arbitrary additive offsets and constant slopes.

Figure shows a typical result for CRISM image 3e12. The topmost figure shows the locations of two samples evidencing strong signals of Olivine and Phyllosilicate respectively. Figures b and c show these two spectra with thick red lines indicating reconstructions from the sparse mixture result. Figure d shows the top constituents recovered for the Olivine site — unsurprisingly each constituent is an instance of Olivine from the source library. Figure e shows top constituents at the Phyllosilicate site. Here a phyllosilicate (Kaolinite, in red) appears alongside two Olivine samples.

We compute abundance maps for Olivine and Phyllosilicate minerals by aggregating the coefficients of all the minerals from each class. Our evaluation compares these to two hand-tuned summary products currently in use by Mars scientists, the OLINDEX and D2300 indicators [2]. These are functions based on slope and band depth that respond strongly

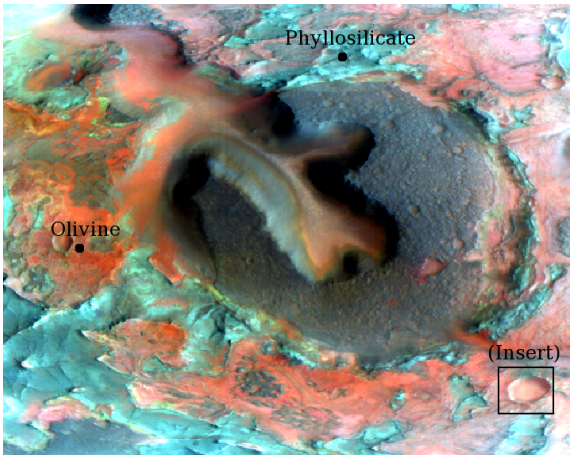

(a) frt00003e12 ($R: 2.0\mu m, G: 1.5\mu m, B: 1.1\mu m$)

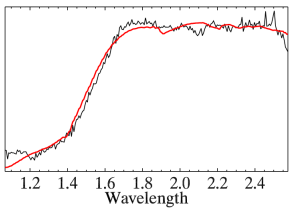

(b) Olivine reconstruction

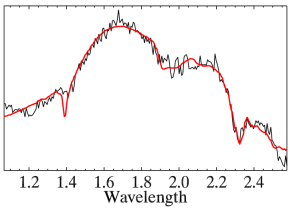

(c) Phyllosil. reconstruction

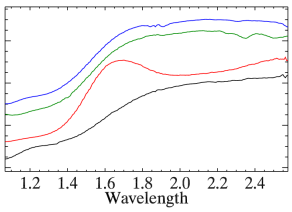

(d) Olivine top sources

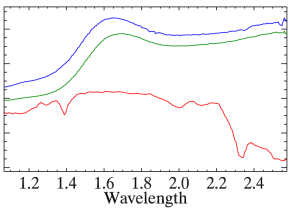

(e) Phyllosilicate top sources

(f) Olivine abundance

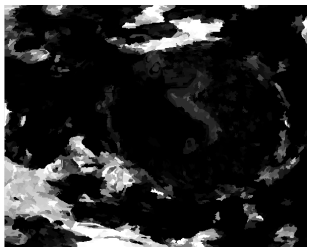

(g) Phyllosilicate abundance

(h) OLINDEX Index

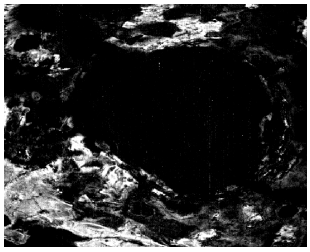

(i) D2300 Index

Fig. 2. Sparse unmixing of CRISM image frt00003e12.

to olivine and phyllosilicates respectively. Figures f-i show abundance maps and corresponding summary products.

We consider both a coarse and fine superpixels with minimum sizes of 20 and 100 pixels for each image. Figure 3 shows correlations between the automated abundance maps and the indicator functions for the two segmentations. The columns, from left to right, show: the mineral type and index used, the CRISM image, the number of superpixels for coarse (C) and fine (F) segmentations, the linear correlation between abundance maps and the selected index, the Spearman's ρ rank correlation coefficient, the precision score, and the recall score. These last two scores are produced by thresholding summary indices and abundance maps at an appropriate level to yield a binary detection decision at each pixel. Precision considers the fraction of automatic detections that are actually present in the summary product, while recall describes the percentage of summary product detections that are automatically recovered. We advise caution in interpreting this result since the summary products themselves do not constitute a ground truth judgment on the presence or absence of a mineral, so in the case of discrepancies either method might be erroneous.

Index	Image	n	corr	ρ	prec	rec
Olivine (OLIND)	3e12	(C) 664	0.87	0.91	0.89	0.81
		(F) 3667	0.90	0.95	0.92	0.83
Olivine (OLIND)	3f8b	(C) 594	0.87	0.90	0.91	0.86
		(F) 3676	0.92	0.94	0.94	0.87
Phyllosil. (D2300)	3e12	(C) 664	0.67	0.46	0.76	0.55
		(F) 3667	0.73	0.49	0.80	0.53

Fig. 3. Comparative evaluation (see text for details).

4. DISCUSSION

The unmixing strategy achieves high correlation with the specific detection algorithms despite being a fully-automated "general" detection method. The unmixing result is fully interpretable; its value traces to a specific unmixing result composed of particular component minerals. Lower correlation and Spearman ρ scores for the Phyllosilicate indicator reflect the smaller percentage of this material in the image; irrelevant low-abundance superpixels dominate the score. The automatic method successfully detects Hydromagnesite in image 3fb9, but we exclude this from our tests since standard carbonate summary products fail to detect this signal.

We have presented preliminary results from an unmixing approach to mineralogical search and survey in large image catalogs. Exponential priors encourage a sparse unmixing solution and a graph-based "superpixel" segmentation compresses high-resolution hyperspectral images for improved speed. Rather than looking for diagnostic slopes or band depths, which may be at or below the level of noise, the unmixing approach computes abundances by generating the mixture to explain the entire spectral waveshape. Leveraging sparse, adaptive unmixing may eventually improve detection sensitivity beyond that offered by static decision rules. We believe the ability to quickly search mineral catalogs with a fully automated, general procedure makes the technique a promising candidate for rapid hyperspectral image analysis.

We performed this research at the Jet Propulsion Laboratory with support from the Advanced Multi-Mission Operations System (AMMOS). Government Sponsorship Acknowledged.

5. REFERENCES

[1] S. Murchie et al., "Compact reconnaissance imaging spectrometer for Mars (CRISM) on Mars reconnaissance orbiter," *J. Geophys. Res*, vol. 112, no. 5, 2007.

[2] S.M. Pelkey et al., "CRISM multispectral summary products: Parameterizing mineral diversity on Mars from reflectance," *J. Geophys. Res*, vol. 112, 2007.

[3] G. W. Patterson et al., "Developing Tools to Highlight the Presence of Carbonates in CRISM Images of Mars," in *Lunar and Planetary Science Conference*, 2009.

[4] C.M. Bishop, *Neural networks for pattern recognition*, Oxford University Press, USA, 1995.

[5] JR Quinlan, "Induction of decision trees," *Machine learning*, vol. 1, no. 1, pp. 81–106, 1986.

[6] D.D. Lee and H.S. Seung, "Algorithms for non-negative matrix factorization," *Advances in neural information processing systems*, pp. 556–562, 2001.

[7] S. Moussaoui et al., "A Bayesian method for positive source separation," in *IEEE International Conference on Acoustics, Speech, and Signal Processing*, 2004.

[8] C. Leng, Y. Lin, and G. Wahba, "A note on the lasso and related procedures in model selection," *Statistica Sinica*, vol. 16, no. 4, pp. 1273, 2006.

[9] X. Ren and J. Malik, "Learning a classification model for segmentation," in *IEEE International Conference on Computer Vision*, 2003, pp. 10–17.

[10] P.F. Felzenszwalb and D.P. Huttenlocher, "Efficient graph-based image segmentation," *International Journal of Computer Vision*, vol. 59:2, pp. 167–181, 2004.

[11] J.F. Mustard et al., "Hydrated silicate minerals on Mars observed by the Mars Reconnaissance Orbiter CRISM instrument," *Nature*, vol. 454, no. 7202, 2008.

[12] B.L. Ehlmann, , et al., "Orbital Identification of Carbonate-Bearing Rocks on Mars," *Science*, vol. 322, no. 5909, pp. 1828, 2008.